

Improved indirect control of nuclear spins in diamond NV centers

Jingfu Zhang, Swathi S. Hegde and Dieter Suter
Fakultaet Physik, Technische Universitaet Dortmund,
D-44221 Dortmund, Germany
(Dated: December 24, 2019)

Hybrid quantum registers consisting of different types of qubits offer a range of advantages as well as challenges. The main challenge is that some types of qubits react only slowly to external control fields, thus considerably slowing down the information processing operations. One promising approach that has been tested in a number of cases is to use indirect control, where external fields are applied only to qubits that interact strongly with resonant excitation pulses. Here we use this approach to indirectly control the nuclear spins of an NV center, using microwave pulses to drive the electron spin, combined with free precession periods optimized for generating logical gate operations on the nuclear spins. The scheme provides universal control and we present two typical applications: polarizing the nuclear spin and measuring nuclear spin free induction decay signals, both without applying radio-frequency pulses. This scheme is versatile as it can be implemented over a wide range of magnetic field strengths and at any temperature.

I. INTRODUCTION

Hybrid quantum systems [1], such as electron-nuclear spins of the nitrogen vacancy (NV) center in diamond [2], have emerged as useful physical systems for implementing quantum computing and imaging [3–7]. The difference in the inherent properties of the two subsystems are often useful, e.g. for implementing fast gate operations on the electron spin and achieving long information storage in the nuclear spin. However, it also provides challenges for the coherent control of hybrid spin systems, e.g. since the interaction between the nuclear spin magnetic moment and the control fields is orders of magnitude weaker than that of the electron spins, which has relatively short coherence times.

The magnetic moment of the nuclear spin can be enhanced by the hyperfine coupling with the electron spin in the NV center [2, 8]. This corresponds to an enhancement in the effective gyromagnetic ratio of the nuclear spin and is determined by the strength of the coupling. For systems with sufficiently strong couplings, like those of the nearest ^{13}C spins to the NV center [8–10], or the ^{14}N spin in the NV center [11–13], the enhancement results in nuclear spin Rabi frequencies that are high enough for direct control of the nuclear spins by the application of radio-frequency fields. However, the enhancement and thus the usefulness of the nuclear spins as qubits decreases dramatically with increasing distance of the nuclear spin from the NV center.

To alleviate this problem, the approach relying on indirect control of the nuclear spins was developed theoretically [14, 15] and experimentally demonstrated in various systems, like the malonic acid radical [16, 17] and NV centers [18–21]. This scheme does not require any radio-frequency pulses and therefore achieves much faster operations on the nuclear spins. Instead, it uses only microwave (MW) pulses acting on the electron spin, combined with free precession under the effect of anisotropic hyperfine interactions. The anisotropic interactions re-

sult in different orientations of the nuclear spin quantization axes for different states of the electron spin, and provide the possibility to achieve indirect control of the nuclear spin by only controlling the electron spin [14, 16]. The basic idea of this scheme is to start with the electron spin initialized, e.g., in the $m_S = 0$ state and the nuclear spin aligned along the corresponding quantization axis, which is close to the z -axis. If a MW pulse changes the state of the electron spin on a timescale that is fast compared to the precession period of the nuclear spin, the nuclear spin remains unchanged during the MW pulse. After the pulse, it is therefore oriented at a nonzero angle from the new quantization axis and starts to precess. The control procedure then consists in finding the best combination of precession periods around the different axes that bring the spin close to the targeted orientation. The control efficiency can be improved by maximizing the angle between the different quantization axes of the nuclear spin [14].

In our present work, we chose a system where the hyperfine couplings are close to the Larmor frequency of the nuclear spin, which optimizes the difference in the orientation of the quantization axes to a value close to 90° . Moreover, unlike the scheme in [14], we generalized the switched control scheme by replacing the 180° pulses by arbitrary operations implemented through pulses with variable flip angles and phases. Such generalization extends the search space for optimizing the pulse sequence parameters, and is useful to improve the control efficiency, e.g., to reduce the number of pulses. In our work, the elementary unitary operations consist of only 2 - 3 rectangular MW pulses separated by delays. Compared to earlier works based on dynamical decoupling [19, 20] or modulated microwave pulses [16, 17] that used hundreds or even thousands of MW pulse segments, this is a dramatic reduction of the control cost.

In this article, we use this scheme to implement operations that occur in many quantum information or imaging tasks: we generate and detect nuclear spin coherence, transfer population between the electronic and nuclear

spins and generate a pseudo-Hadamard gate on the nuclear spin. Using these operations, we polarize the nuclear spin and measure the nuclear spin transition frequencies using free induction decay (FID) signals. Our system of interest consists of the electron spin and one ^{13}C nuclear spin, which is relatively weakly coupled to the electron ($A < 0.2$ MHz). In this system, the nuclear spin transition frequencies (NMR spectrum) are spread over a spectral range of more than 200 kHz, which would be out of reach for direct radio-frequency excitation but can be readily excited by our indirect control scheme.

II. SYSTEM AND OPERATIONS TO IMPLEMENT

The spin system consists of the electron, the ^{14}N nuclear spin and one ^{13}C nuclear spin. In this context, we do not consider the ^{14}N spin but focus on the subsystem where the ^{14}N is (and remains) in the $m_N = 1$ state. The spins interact with a weak magnetic field B oriented along the symmetry axis of the NV-center. In a suitable reference frame (for details see Appendix A), we can write the relevant part of the Hamiltonian as

$$\frac{\mathcal{H}_{e,C}}{2\pi} = DS_z^2 - (\nu_e - A_N)S_z - \nu_C I_z + A_{zz}S_z I_z + A_{zx}S_z I_x,$$

where S_z denotes the electron spin-1 operator, and $I_{x/z}$ the ^{13}C spin-1/2 operators. The zero-field splitting is $D = 2.87$ GHz and $\nu_{e/C} = \gamma_{e/C}B$ denote the Larmor frequencies of the electron and ^{13}C nuclear spins and γ the gyromagnetic ratios. $A_N = -2.16$ MHz is the secular part of the hyperfine coupling with the ^{14}N nuclear spin while A_{zz} and A_{zx} are the relevant components of the ^{13}C hyperfine tensor.

The eigenstates of $\mathcal{H}_{e,C}$ are $|1, \varphi_+\rangle, |1, \psi_+\rangle, |0, \uparrow\rangle, |0, \downarrow\rangle, |-1, \varphi_-\rangle$, and $|-1, \psi_-\rangle$, where $|\uparrow\rangle$ and $|\downarrow\rangle$ are the eigenstates of I_z ,

$$\begin{aligned} |\varphi_\pm\rangle &= |\uparrow\rangle \cos(\theta_\pm/2) + |\downarrow\rangle \sin(\theta_\pm/2) \\ |\psi_\pm\rangle &= -|\uparrow\rangle \sin(\theta_\pm/2) + |\downarrow\rangle \cos(\theta_\pm/2) \end{aligned} \quad (1)$$

are the nuclear-spin eigenstates and

$$\theta_\pm = \arctan \frac{A_{zx}}{A_{zz} \mp \nu_C} \quad (2)$$

are the angles between the nuclear spin quantization axis and the z -axis of our coordinate system for the subsystems where the electron spin is in the state $m_S = \pm 1$. $|1\rangle, |0\rangle$ and $|-1\rangle$ are the eigenstates of S_z . Additional details are given in Appendix A. The nuclear spin transition frequencies are ν_C and $\nu_\pm = \sqrt{A_{zx}^2 + (\nu_C \mp A_{zz})^2}$ if the electron spin is in the state $m_S = 0$, and $m_S = \pm 1$, respectively. In the following, we use the eigenstates $\{|0\rangle, |-1\rangle\} \otimes \{|\uparrow\rangle, |\downarrow\rangle\}$ of the operators S_z and I_z as our computational basis.

The experiments were performed at room temperature. We used a ^{12}C -enriched diamond crystal with a ^{13}C concentration of 0.002% [22, 23] and applied a magnetic field

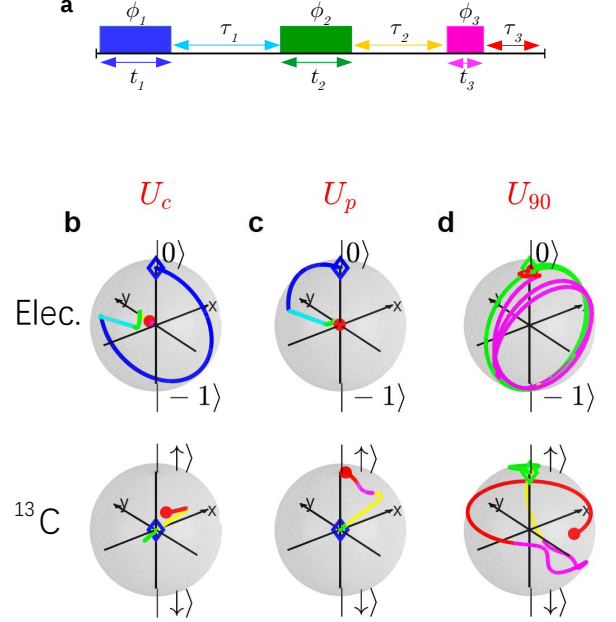


FIG. 1: Pulse sequence and Bloch sphere representation for the evolution of the electron- and ^{13}C spins. (a) MW pulse sequence at a fixed power with the carrier frequency set to the ESR transition frequency $m_S = 0 \leftrightarrow -1$. The pulse durations, phases and delays are indicated as t_k , ϕ_k , and τ_k respectively. (b-d) Evolution trajectories of the electron and ^{13}C spin on the Bloch sphere under the operations U_c , U_p and U_{90} . The initial and final states are indicated by diamonds and filled circles, respectively. In Fig. (b), U_c maps ρ_0 to ρ_c , corresponding to a mixed electron state and a maximum possible ^{13}C coherence. In (c), U_p swaps the states between the electron and ^{13}C . In (d), the electron and ^{13}C spins are both initially in state $|0\rangle$. Under U_{90} , the ^{13}C spin evolves towards the $-y$ -axis, while the electron returns to its initial state. Here U_{90} consists of only 2 MW pulses and 2 delays, i.e., $t_1 = \tau_1 = 0$ in Fig. (a). The color of each partial trajectory corresponds to the color in (a). The parameters of these operations are given in Appendix B. The x , y and z components of the final states on the Bloch sphere are presented in Table IV in Appendix D.

$B = 14.8$ mT. We selected a center with a resolved coupling to a ^{13}C nuclear spin, with the coupling constants $A_{zz} = -0.152$ MHz and $A_{zx} = 0.110$ MHz. For this center, the quantization axis of the nuclear spin is oriented at an angle $\theta_+ = -10^\circ$, $\theta_- = 86^\circ$ and $\theta_0 \approx 0$ from the z -axis if the electron spin is in the ± 1 or 0 state. The MW pulses had a Rabi frequency of ≈ 0.5 MHz, which is small compared to A_N and to ν_e . Accordingly, they only drive the transition from the $m_S = 0$ to one of the $m_S = \pm 1$ states and are selective for $m_N = 1$.

As initial examples of the indirect control approach, we implement three state-to-state transfer operations to which we refer as U_c , U_c^\dagger , and U_p , and one unitary operation, U_{90} . The initial state for the first three operations

is

$$\rho_0 = |0\rangle\langle 0| \otimes E/2, \quad (3)$$

where E is the 2×2 identity operator. This state corresponds to the electron spin in a pure state and the ^{13}C nuclear spin in the maximally mixed state.

We first consider the operations U_c and U_c^\dagger , where U_c converts ρ_0 into nuclear spin coherence in the manifolds $m_S = 0$ and $m_S = -1$ of the electron spin and U_c^\dagger transfers the coherence back to population in $m_S = 0$. The target state of the operation U_c is

$$\rho_c = U_c \rho_0 U_c^\dagger = \frac{1}{2}(|0\rangle\langle 0| \otimes |s_0\rangle\langle s_0| + |-1\rangle\langle -1| \otimes |s_- \rangle\langle s_-|) \quad (4)$$

where

$$\begin{aligned} |s_0\rangle &= (|\uparrow\rangle + i|\downarrow\rangle)/\sqrt{2} \\ |s_- \rangle &= (|\varphi_- \rangle - |\psi_- \rangle)/\sqrt{2} \end{aligned} \quad (5)$$

denote superpositions of the nuclear spin in the energy eigenbasis of the manifolds $m_S = 0$ and -1 .

U_p implements a selective population transfer. It transforms the initial state ρ_0 to

$$\rho_p = U_p \rho_0 U_p^\dagger = \frac{1}{2}(|0\rangle\langle 0| + |-1\rangle\langle -1|) \otimes |\uparrow\rangle\langle \uparrow|, \quad (6)$$

where the electron spin is in the maximally mixed state in the subspace $m_S = \{0, -1\}$ while the nuclear spin is in the pure state $|\uparrow\rangle$. Clearly U_p implements a SWAP operation that aligns the nuclear spin along the z -axis.

To implement the operation U_c , U_c^\dagger or U_p , we search for pulse sequence that maximizes the overlap between the final state and the target state. We use a MATLAB[®] subroutine based on a genetic algorithm [24] to find the optimal set of parameters. The third operation $U_{90} = e^{-i(\pi/2)I_x}$ is a $\pi/2$ rotation around the x -axis for ^{13}C , or a pseudo-Hadamard gate, since it is equivalent to the Hadamard gate U_H up to operations around the z -axis as

$$U_H = ie^{-i(\pi/2)I_z} U_{90} e^{-i(\pi/2)I_z}, \quad (7)$$

where the z -rotations can be easily absorbed in a suitable reference frame shift [25, 26]. For U_{90} , we maximize the process fidelity of the gate. Fig. 1 (a) illustrates the pulse sequence, where the pulse durations t_k , phases ϕ_k , and the durations τ_k of the free precession periods were used as adjustable parameters in the optimization.

To obtain sequences that are robust against fluctuations of the MW power, we averaged the fidelities over a range of MW field amplitudes, as described in the Appendix B. We obtained theoretical state fidelities of 95% for the target states of U_c and U_c^\dagger , and 98% for U_p with sequences of 3 pulses and 3 delays, and gate fidelity of 92% for U_{90} with a sequence of 2 pulses and 2 delays. The total duration of these pulse sequences is $\approx 7 - 15\mu\text{s}$, shorter than the transverse relaxation time $T_2^* \approx 20\mu\text{s}$ of the electron spin. Figs. 1(b-d) show the evolution of the electron and ^{13}C spins during the pulse sequence on the Bloch sphere during these pulse sequences.

III. EXPERIMENTAL RESULTS

The experimental scheme to measure ^{13}C transition frequencies via indirect FID measurement in electron subspaces of $m_S = \{0, -1\}$, and the pictorial representations of the state evolution are shown in Figs. 2 (a, b). The first laser pulse initializes the system to state ρ_0 . This is followed by the generation of ^{13}C coherence using U_c as indicated by the wavelike patterns in Fig. 2 (b). ρ_c then evolves freely for a time τ . U_c^\dagger converts the final coherence back to population of $m_S = 0$. The last laser pulse is used to measure the population of $m_S = 0$, and generates a signal proportional to

$$P_{|0\rangle} = \text{Tr}\{\rho_c \rho_\tau\} = [\cos(2\pi\nu_C\tau) + \cos(2\pi\nu_-\tau)]/8 + 1/4 \quad (8)$$

with $\rho_\tau = e^{-i\tau\mathcal{H}_{e,C}} \rho_c e^{i\tau\mathcal{H}_{e,C}}$.

Figs. 2 (c-d) show the experimental scheme and state representations for the ^{13}C FID in $m_S = \{-1, 1\}$. It starts with the same sequence as in (a) to put the system in to the state ρ_c . A first 180° pulse applied to the $m_S = 0 \leftrightarrow 1$ transition then transforms ρ_c into

$$\rho'_c = (|1\rangle\langle 1| \otimes |s_0\rangle\langle s_0| + |-1\rangle\langle -1| \otimes |s_- \rangle\langle s_-|)/2. \quad (9)$$

In the $m_S = 1$ state, the nuclear spin quantization axis is almost parallel to the z -axis ($\theta_+ \approx 0^\circ$). Therefore, the nuclear spin coherence remains an almost equal weight superposition of the two eigenstates, which subsequently undergoes free evolution for a time τ . After the free evolution, the second 180° pulse exchanges again the states $m_S = 1$ and $m_S = 0$ and U_c^\dagger works in the same manner as in Fig. 2 (a). The signal generated after the last laser pulse is proportional to

$$P'_{|0\rangle} = \text{Tr}\{\rho'_c \rho'_\tau\} = [\cos(2\pi\nu_-\tau) + \cos(2\pi\nu_+\tau)]/8 + 1/4 \quad (10)$$

with $\rho'_\tau = e^{-i\tau\mathcal{H}_{e,C}} \rho'_c e^{i\tau\mathcal{H}_{e,C}}$.

Figs. 2 (e-f) show the resulting ^{13}C spectra, obtained by Fourier transformation of the FID data which are presented in Fig. 12 in the Appendix D. Since ρ_c and ρ'_c contain coherence in two different NMR transitions, each of the resulting spectra features two resonance lines. The measured transition frequencies are 0.159, 0.111, and 0.328 MHz and agree well with the analytical solutions for ν_C , ν_- and ν_+ respectively. The linewidths are not the natural linewidths but are determined by the truncation of the FID signal. Since the FID for Fig. 2 (f) was measured for $300\mu\text{s}$ and that for (e) for $200\mu\text{s}$, the resonance lines in (f) are slightly narrower. More details are presented in Appendix D.

As yet another illustration, we use U_p to polarize ^{13}C - a necessary step in realizing quantum computation [9, 18, 19, 27–31]. Figs. 3 (a-b) show the experimental scheme and a schematic representation of the states during the intermediate steps. After the initialization step, U_p transforms ρ_0 to ρ_p , see Eq. (6). The laser pulse in the polarization step resets the electron from $m_S = -1$ back to $m_S = 0$. To measure the populations of states

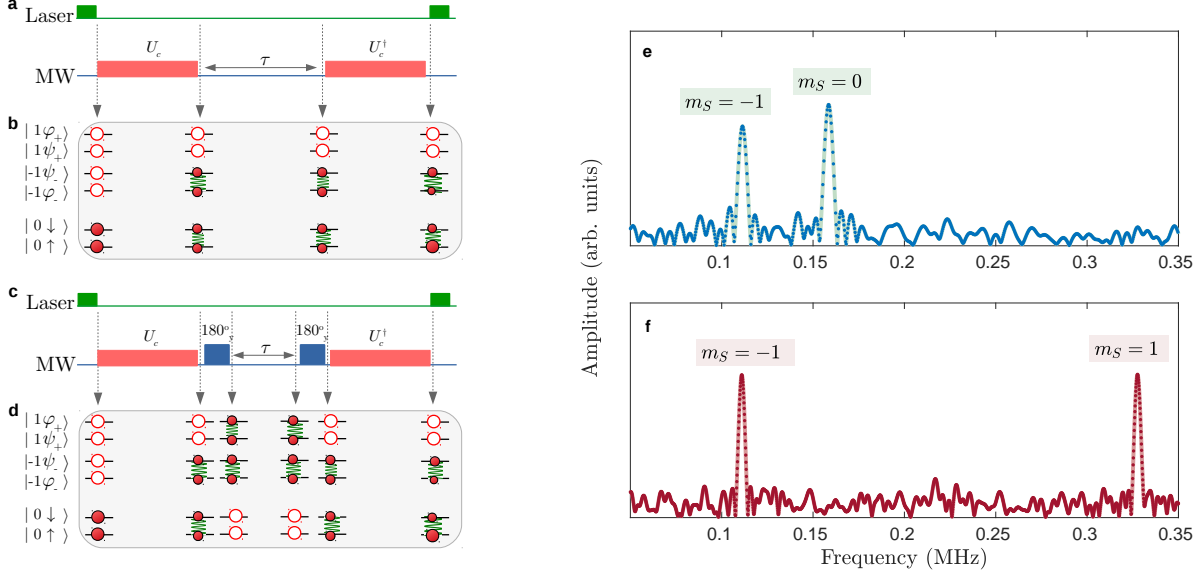


FIG. 2: Experimental schemes and results for generating and detecting coherence in ^{13}C spin via indirect control. (a, c) Pulse sequences. The red rectangles denote MW pulse sequences resonant with transition $m_S = 0 \leftrightarrow -1$ to implement the operations U_c and U_c^\dagger , as indicated above the rectangles. The blue rectangles denote 180° -pulses resonant with transition $m_S = 0 \leftrightarrow 1$ in the $m_N = 1$ subspace. The first laser pulse initializes the electron and ^{13}C in state ρ_0 . U_c transforms ρ_0 to ρ_c . ρ_c or ρ_c' then undergoes free evolution for time τ and U_c^\dagger transfers the evolved coherence back to population of the $m_S = 0$ state. During the second laser pulse, photon counting measures this population. (b, d) Schematic representations of the state evolution at each stage of the operation. The filled circles represent the populations and the wavelike patterns represent coherence. (e-f) Spectra of the ^{13}C spin, measured with the sequences (a) and (c), respectively. The states of electron spin are indicated in the panels for each resonance line.

$|0, \uparrow\rangle$ and $|0, \downarrow\rangle$, denoted as $P_{|0\uparrow\rangle}$ and $P_{|0\downarrow\rangle}$, in the $m_S = 0$ subsystem, we performed the standard FID experiment on the electron spin, followed by a detection laser pulse. In the obtained ESR spectrum, the amplitudes of the resonance lines are proportional to the populations $P_{|0\uparrow\rangle}$ and $P_{|0\downarrow\rangle}$, respectively.

Fig. 3 (c) shows the spectra obtained from ρ_0 (as a reference) and ρ_p , when the laser pulse in the polarization step was switched off. In the spectrum from ρ_p , the population of state $|0, \downarrow\rangle$ was almost completely moved away, shown as the negligibly small left peak. Ideally, the right peak should have the same height as in the unpolarized state spectrum. The ratio of the two peak amplitudes is ≈ 0.92 , which we use as a measure of the fidelity of the implemented U_p .

Fig. 4 shows the experiment result for polarizing the ^{13}C spin with a laser pulse of duration $d_L = 1.1 \mu\text{s}$. The corresponding spectrum for the unpolarized ^{13}C spin is also shown as a reference. The inset shows the nuclear spin polarization $p = P_{|0\uparrow\rangle} - P_{|0\downarrow\rangle}$ as a function of the laser pulse duration, for a laser power of about 0.5 mW. It can be fitted by the function

$$p_{\text{repol}} = 0.31 - 0.51e^{-(\alpha+\beta)d_L} + 0.50e^{-2\gamma d_L} \quad (11)$$

where $\alpha = 1.10 \mu\text{s}^{-1}$, $\beta = 0.41 \mu\text{s}^{-1}$ and $\gamma = 0.022 \mu\text{s}^{-1}$ are the pumping rates for states $|-1, \uparrow\rangle \rightarrow |0, \uparrow\rangle$

(or $|-1, \downarrow\rangle \rightarrow |0, \downarrow\rangle$), $|-1, \uparrow\rangle \rightarrow |0, \downarrow\rangle$ (or $|-1, \downarrow\rangle \rightarrow |0, \uparrow\rangle$), and $|0, \uparrow\rangle \leftrightarrow |0, \downarrow\rangle$, respectively [9]. The highest polarization of $p_{\text{max}} \approx 80\%$ was reached for a laser pulse duration d_L around $1.1 \mu\text{s}$.

In the following, we use this polarized state to demonstrate the pseudo-Hadamard gate U_{90} . We detect its effect by implementing the standard ^{13}C FID experiment (see, e.g., [9, 11]). The MW pulse sequences and experimental results are shown in Fig. 5. Unlike in subspace $m_S = 0$, we replace U_{90} by a 180_y° MW pulse that transforms $m_S = 0$ to -1 , and generates a coherence between $|\psi_-\rangle$ and $|\varphi_-\rangle$ of ^{13}C in $m_S = -1$ subspace since $\theta_- \approx 90^\circ$. The scheme for the $m_S = 1$ subspace is similar to the case of $m_S = 0$, except that we transfer the spin states between $m_S = 0$ and $m_S = 1$ by 180_y° pulses before and after the free evolution time τ . The measured transition frequencies are measured as 0.158, 0.110 and 0.328 MHz, matching well with ν_C , ν_- and ν_+ .

The performance of the operations U_c and U_{90} can be evaluated by analyzing the signals shown in Figs. 2 and 5, combined with numerical simulation. The experimental fidelities for U_c and U_{90} are 0.91 and 0.74, respectively. The details are presented in Appendix C. The theoretical infidelities for the sequences are 0.02, 0.05, and 0.08, for U_c , U_p and U_{90} . The excess infidelities can be attributed to relaxation effects of the electron spin and pulse imper-

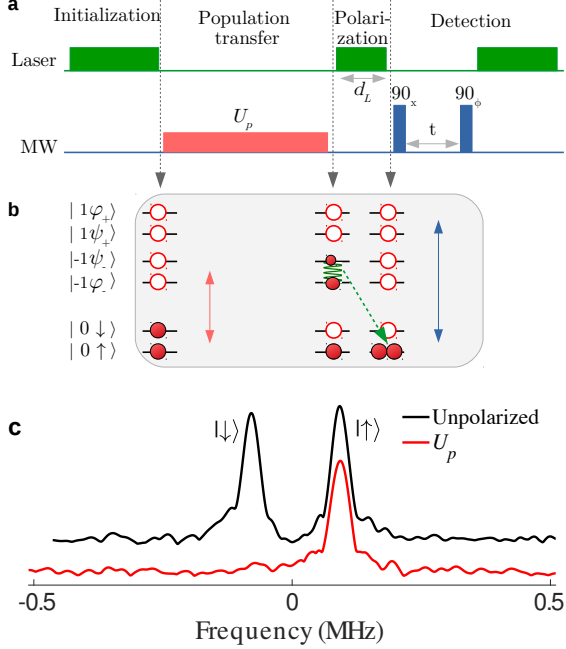


FIG. 3: Polarization scheme and experimental results. (a) Pulse sequence. In the initialization step, the electron and ^{13}C spins are set into state ρ_0 . For the population transfer, we apply MW pulses to transfer the population from states $|0, \downarrow\rangle$ to $|-1, \uparrow\rangle$. In the polarization step, a laser pulse resets the electron from $m_S = -1$ back to $m_S = 0$. We then measure an electron spin FID on the transition $m_S = 0 \leftrightarrow m_S = 1$ to determine the populations of the carbon spin states $|\uparrow\rangle$ and $|\downarrow\rangle$. Here we use MW pulses with a Rabi frequency of 3.7 MHz to reduce the operation time, since the selectivity for the subspace of ^{14}N state is not required. The peaks of other ^{14}N states are also observed but not shown here. (b) Schematic representation of the state during the intermediate steps in (a). The filled circles denote the population size. The short (long) vertical double arrows indicate the transition $m_S = 0 \leftrightarrow -1$ ($m_S = 0 \leftrightarrow 1$). (c) ESR spectra of the $m_S = 0 \leftrightarrow 1$ transition obtained from states ρ_0 and ρ_p when $d_L = 0$, where the ^{13}C spin is unpolarized (thermal) and in state $|\uparrow\rangle$, indicated by the black and red curves, respectively.

fections.

IV. DISCUSSION

A. The coupled ^{14}N

Since our interests in the current work focuses on the control of the electron and ^{13}C spins, perturbing effects from the ^{14}N , which is also coupled to the electron spin should be minimized. For this purpose, we have chosen a suitable strength of the MW pulses, such that the Rabi frequency of the MW pulses is strong enough compared with the couplings of the ^{13}C , but weak enough to affect

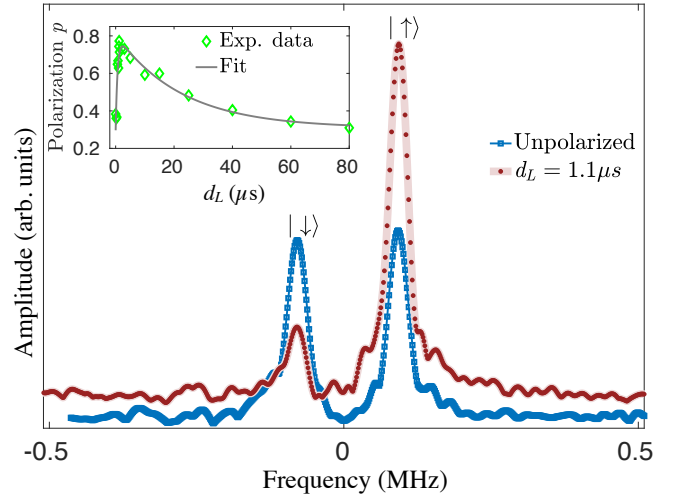


FIG. 4: ESR spectra of the $m_S = 0 \leftrightarrow 1$ transition when the ^{13}C spin is in the unpolarized state and when it is polarized with a laser pulse of duration $d_L = 1.1 \mu\text{s}$ resulting in a polarization $p \approx 80\%$. In inset shows the dependence of the population difference p on the laser pulse duration d_L .

	U_p		U_{90}	
Rabi (MHz)	Fidelity	Duration (μs)	Fidelity	Duration (μs)
0.2	0.996	8.65	0.82	13.9
0.5	0.997	7.85	0.97	13.4
10	0.998	7.65	0.99	13.1

TABLE I: Simulated results for the dependence of the fidelity and total duration of the operations U_p and U_{90} on the Rabi frequency of the MW pulses.

only one subspace of the ^{14}N [32]. This strategy works well for the case where the couplings of the ^{13}C are even weaker, and the MW strength can be further reduced to improve the selectivity for the subspace [33]. However, for the case where the couplings of the ^{13}C are comparable or even higher than the coupling from the ^{14}N , the selection of the subspace becomes more challenging. For this case, one of the alternatives is to polarize the ^{14}N [34, 35], e.g., to the state $m_N = 1$, so that the ^{14}N only contributes a fixed frequency shift, and high power (or hard) MW pulses can be used. Obviously the effects of the coupled ^{14}N depend on the achieved polarization of the ^{14}N . Recent results show that a polarization of $> 98\%$ can be reached [31].

We used numerical simulations to investigate the fidelity and duration of the operations U_p and U_{90} for different Rabi frequencies. The results are listed in Table I. For U_p , the results are not sensitive to the Rabi frequency. For U_{90} , higher Rabi frequencies lead to higher fidelities, with similar total sequence length. In these simulations, the pulse sequences are not robust against the fluctuation of the MW power, and therefore the theoretical fidelities at 0.5 MHz Rabi frequency are higher than the robust sequences used in the experiment.

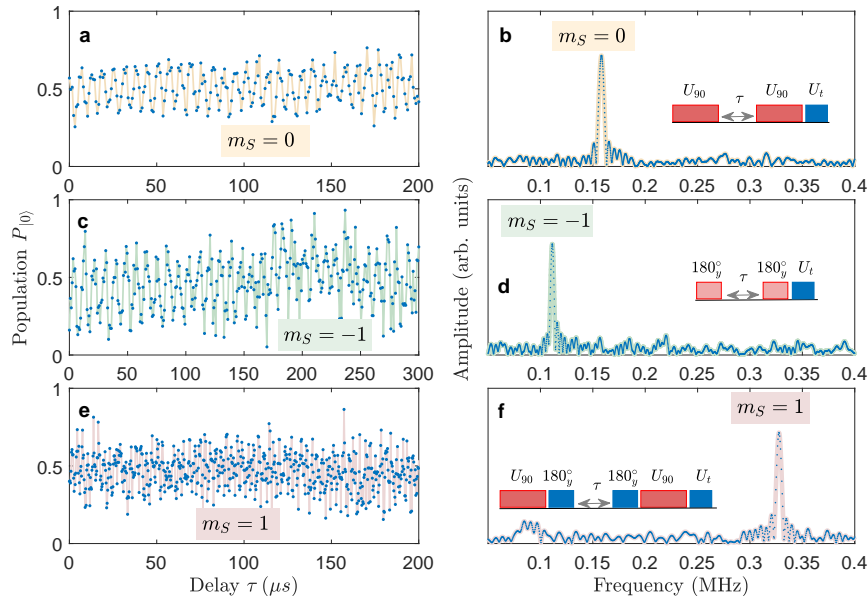


FIG. 5: Experimental ^{13}C FIDs obtained with the transformation U_{90} . The time domain data and the Fourier transforms are shown as the left to right columns. From top to bottom we list the results obtained in the subspaces $m_S = 0, -1, 1$, and the insets show the MW pulse sequences correspondingly. U_t performs as a controlled NOT -like gate approximately in the subspace spanned in the basis $\{m_S = 0, m_S = 1\} \otimes \{|\uparrow\rangle, |\downarrow\rangle\}$ to transfer the population from state $|0, \downarrow\rangle$ to $|1, \downarrow\rangle$ [32], so that the ^{13}C coherence can be detected by the readout laser. U_t is implemented by two 90° MW pulses with 90° phase shift and separated by a delay of $1/(2|A_{zz}|)$.

	U_p		U_{90}	
Rabi (MHz)	Fidelity	Duration (μs)	Fidelity	Duration (μs)
10	0.65	6.5	0.99	13.1
0.5	0.61	10-17	0.97	13.5

TABLE II: Results obtained by simulation using the theoretical scheme proposed in Ref. [14]. In the optimization for U_p or U_{90} , we used the same numbers of the pulses and delays in the pulse sequence shown in Fig. 8, except that we fixed the flip angles for each pulse to 180° .

B. Comparison with the previous work

In previous works based on dynamical decoupling (DD) [19, 20], multiple cycles of the DD sequences were applied. The delay time between the DD pulses was determined by DD spectroscopy, and the weak coupling condition was used, where the hyperfine coupling is small compared to the Larmor frequency of the nuclear spin. In our system, however, the Larmor frequency ν_C is close to the hyperfine coupling, violating this condition.

In Ref. [21], the proximal ^{13}C spin was studied, where the hyperfine coupling is much larger than the Larmor frequency. In this case, it is possible to generate a large angle between the nuclear quantization axes of the man-

ifolds $m_S = 0$ and $m_S = -1$ by choosing a suitable angle between the static field and the NV axis. The DD pulses were used to flip the states of the electron spin. Compared with this work, the hyperfine coupling in our work is much weaker, and the Rabi frequency of the nuclear spin cannot be observed in our experimental setup.

Using the theoretical procedure outlined in Ref. [14], we simulated the short sequences of MW pulses but fixed the flip angle for each pulse to 180° . We checked the optimization for U_p and U_{90} . The results of the simulation are listed in Table II. For U_p , the fidelity is quite low, which indicates that this method does not work for U_p . For U_{90} , however, we obtained useful results as listed in Table II. These results illustrated the similarity between our pulse optimization and the switched control in Ref. [14]. Such similarity can also be noticed in the pulse sequence for U_{90} used in the experiment, shown in Fig. 8 in Appendix B, where the flip angles are effectively close to 180° .

C. Number of MW pulses

Using more pulses and delays provides additional parameters for the optimization of the pulse sequences and can therefore result in higher theoretical fidelities. In

Number of pulses	Fidelity	Duration (μs)
3	0.86	11.6
4	0.976	13.5
5	0.997	8.89

TABLE III: Results of the optimisation of U_p , for $\theta_- = 36.6^\circ$.

a typical implementation, however, they lead to longer sequences and therefore aggravate losses of the fidelity through decoherence. Moreover, the additional pulses also introduce additional errors from pulse imperfections. In the present system, we found that sequences with 2-3 pulses are a good compromise.

Using numerical simulations, we investigated the dependence of the fidelity and operation duration on the number of MW pulses. For U_{90} , using 3 pulses, we can improve the fidelity to 0.99. This result is consistent with the theoretical prediction [14]. However, the operation duration is about 32 μs , twice as long as with 2 pulses (see Fig. 8 in Appendix B), and exceeds the transverse relaxation time of the electron spin. The control pulses may thus have to be combined with DD pulses, as illustrated in previous works [19–21].

The number of pulses that is required to implement a specific operation depends on the angle between the nuclear spin quantization axes in the different electron spin eigenstates. We demonstrate this with a simulation for the present system: if we change the static magnetic field to 28 mT, the ^{13}C Larmor frequency becomes 0.3 MHz and the angle θ_- changes to 36.6° , while θ_0 does not change. Table III lists the results for the operation U_p for a Rabi frequency of $\omega_1 = 0.5$ MHz. Here, the optimal number of pulses is 5, which is consistent with the theoretical prediction that number of rotations required is not more than 6 [14]. The pulse sequences are shown as Fig. 9 in Appendix B.

V. CONCLUSION

We have demonstrated highly efficient control of nuclear spins in a solid-state system without using any radio-frequency irradiation. Instead, we relied on suitably chosen sequences of microwave pulses that drive the electronic spin and thereby modulate the anisotropic interaction and the effective field acting on the nuclear spins. The scheme was verified for the example of diamond NV-centers, working at room temperature. Using this technique, we implemented several fundamental unitary operations for quantum computing, such as generating quantum coherence, transferring populations, and Hadamard-like gate. For this demonstration, we only used 2 or 3 MW control pulses, resulting in short gate times. Our scheme does not require a specific choice of the magnetic field, it can be used at arbitrary temperature and applied to different types of hybrid qubit systems.

Acknowledgement This work was supported by the DFG

through grants SU 192/34-1 and SU 192/19-2. We thank Daniel Burgarth for helpful discussions.

Appendix

A. System, Hamiltonian and ESR Spectra

We consider the spin system consisting of the electron, the ^{14}N nuclear spin and one ^{13}C nuclear spin. The axis of the NV system, together with the position of the ^{13}C nucleus define a symmetry plane for the system [8]. We therefore use a symmetry-adapted coordinate system, where the z -axis is oriented along the NV axis, while the ^{13}C nucleus is located in the xz -plane, as shown in Fig. 6 (a). The static magnetic field \vec{B} is aligned along the NV symmetry axis so as to simplify the Hamiltonian and to maximize the electron spin polarization [36]. The relevant Hamiltonian is then

$$\begin{aligned} \mathcal{H}/(2\pi) = & DS_z^2 - \nu_e S_z + P(I_z^N)^2 - \nu_N I_z^N - \nu_C I_z \\ & + A_N S_z I_z^N + A_{zz} S_z I_z + A_{zx} S_z I_x. \end{aligned} \quad (12)$$

The symbols for the electron spin \vec{S} and the ^{13}C nuclear spin \vec{I} are defined in the main text. I_z^N denotes the spin-1 operator for ^{14}N , which experiences a nuclear quadrupole splitting with coupling constant $P = -4.95$ MHz and a hyperfine interaction with coupling constant $A_N = -2.16$ MHz [37–39]. Fig. 6 (b-f) show the energy levels and ESR spectra.

If we focus on a subspace where the state of the ^{14}N is fixed ($m_N = 1$ in the main text), $\mathcal{H}_{e,C}$ can be diagonalized by the unitary transformation

$$U_T = |1\rangle\langle 1| \otimes R_y(\theta_+) + |0\rangle\langle 0| \otimes E + |-1\rangle\langle -1| \otimes R_y(\theta_-), \quad (13)$$

where $R_y(\theta_\pm) = e^{-i\theta_\pm I_y}$. The four ESR transitions $m_S = 0 \leftrightarrow \pm 1$ appear then $D \mp (\nu_e - A_N)$, shifted by

$$\frac{1}{2}(\nu_\pm + \nu_C), -\frac{1}{2}(\nu_\pm - \nu_C), \frac{1}{2}(\nu_\pm - \nu_C), -\frac{1}{2}(\nu_\pm + \nu_C), \quad (14)$$

where the upper / lower sign indicates that they are associated with the $m_S = \pm 1$ states, respectively. The corresponding transition probabilities are

$$\sin^2(\theta_\pm/2), \cos^2(\theta_\pm/2), \cos^2(\theta_\pm/2), \sin^2(\theta_\pm/2) \quad (15)$$

respectively.

B. Pulse Sequences

In a subspace spanned by the states

$$\{|0\rangle, |-1\rangle\}_e \otimes \{|1\rangle\}_N \otimes \{|\uparrow\rangle, |\downarrow\rangle\}_C, \quad (16)$$

the Hamiltonian of the electron- ^{13}C system can be represented as

$$\frac{1}{2\pi} \mathcal{H}_s = (-\nu_C - \frac{A_{zz}}{2}) I_z + A_{zz} s_z I_z + A_{zx} s_z I_x - \frac{A_{zx}}{2} I_x \quad (17)$$

in the rotating frame with frequency $D + \nu_e - A_N$, where s_z denotes the pseudo-spin 1/2 operator for electron spin. We consider pulse sequences consisting of n MW pulses with fixed Rabi frequency ω_1 , as shown in Fig. 7. The propagators for the individual MW pulses can be written as $U_k^{MW} = e^{-i\mathcal{H}_k^{MW}t_k}$ where $\mathcal{H}_k^{MW} = \mathcal{H}_s + \omega_1[s_x \cos(\phi_k) + s_y \sin(\phi_k)]$, and for the free evolutions as $U_k^d = e^{-i\mathcal{H}_s\tau_k}$, with $k = \{1, \dots, n\}$. The total unitary U is a time ordered product of the U_k^{MW} and U_k^d , and is a function of the pulse parameters $(t_1, \dots, t_n, \phi_1, \dots, \phi_n, \tau_1, \dots, \tau_n)$. The goal is to design U with suitable pulse parameters such that the fidelity $F_g = |\text{Tr}(U_T^\dagger U)|/4$ of the effective propagator U with respect to the target propagator U_T is maximized. We used a genetic algorithm as a numerical search method to obtain the best pulse parameters.

For some applications, we do not have to find a specific unitary propagator, but it is sufficient to transfer a given initial state ρ_0 to a target state ρ_T . The actual final state is then $\rho_{opt} = U\rho_0 U^\dagger$, where $\rho_{opt} \equiv \rho_{opt}(t_1, \dots, t_n, \phi_1, \dots, \phi_n, \tau_1, \dots, \tau_n)$, and we maximize the state fidelity $F_s = \text{Tr}(\rho_T \rho_{opt}) / \sqrt{\text{Tr}(\rho_T^2) \text{Tr}(\rho_{opt}^2)}$.

The performance of the pulses is sensitive to variations in ω_1 . To obtain good fidelity in experiments where the actual MW amplitude deviates from the ideal one, we optimized the pulse sequences for a range of amplitudes, taking the average fidelity as the performance measure. For the gates U_c , U_c^\dagger and U_p , we used the range $\omega_1/2\pi = [0.47, 0.53]$ MHz and for U_{90} $\omega_1/2\pi = [0.48, 0.52]$ MHz. The optimized pulse sequences for U_c , U_c^\dagger , U_p and U_{90} are shown in Fig. 8. The theoretical robust state fidelities for the four sequences are 95%, 95%, 98% and 92%, respectively.

In Fig. 9, we illustrate a pulse sequence to implement U_p for the case of $\nu_C = 0.3$ MHz, by increasing the static magnetic field.

C. Experimental performance of U_{90} and U_c

1. U_{90}

We can exploit the measured populations $P_{|0\rangle}$ shown in Figs. 5 (a), (c) and (e) to estimate experimental fidelity of U_{90} . Here we chose the data in initial parts, since the signals in these periods are less noisy. Then we fit the data points using a function as $a_{m_S} + b_{m_S} \sin(2\pi\nu_{m_S}\tau + c_{m_S})$, shown in Fig. 10. Here ν_{m_S} denotes the transition frequency measured in the spectra shown in Figs. 5(b, d, f), respectively, with the index indicating the involved subspace. The parameters a_{m_S} , b_{m_S} and c_{m_S} are constants in each subspace.

We used the ratios between b_{m_S} to estimate the experimental fidelities for U_{90} as well as the 180° MW pulse in the insets in Figs. 5(d-f) as the following. In this manner, we can eliminate the errors in the operation of polarizing the ^{13}C spin and the detection operation U_t . The fitted b_{m_S} is listed as 0.13, 0.11 and 0.20 for $b_{m_S} = 0, 1$ and -1 , respectively. Noticing the pulse sequences shown as the insets in Figs. 5(b) and (f), we can obtain the fidelity for the 180° MW pulse in the inset (f) as $F_{180} = \sqrt{b_1/b_0} = 0.92$. In a similar way, we then obtained the fidelity for U_{90} as $F_{U_{90}} = \sqrt{b_1/b_{-1}} = 0.74$. Here we assumed that the 180° pulses in insets (d-f) have the same fidelity.

2. U_c

In this section, we evaluate the performance of the operation U_c using the experimental ^{13}C spin spectrum in Fig. 2 (f) measured with the pulse sequence shown in Fig. 2 (c). We then compare this experimental spectrum with the corresponding theoretical spectrum. The theoretical population at the end of this pulse sequence is $P'_{|0\rangle}$ and its dependence on the delay τ is explained as Eq. (10) in the main manuscript. The Fourier transformation of $P'_{|0\rangle}$ in the frequency domain is $y(\nu) = \mathcal{F}\{P'_{|0\rangle}\}$. We fit this theoretical spectrum to the experimental spectrum by multiplying $y(\nu)$ by a factor $f = 0.7$. This fit is shown in Fig. 11. Following this result, we can estimate the experimental fidelity for U_c and U_c^\dagger as $F_{U_c} = \sqrt{f}/F_{180} = 0.91$, where U_c^\dagger is assumed the same as U_c .

D. Other supplementary data

In Table IV, we list the components of the final states on the Bloch sphere shown in Fig. 1.

In Figs. 12 (a-b), we illustrated the FID signals of ^{13}C obtained by the pulse sequences shown as Figs. 2 (a) and (c), respectively. The corresponding spectra are shown in Fig. 2 (e-f). In experiment we optimized the duration of the FID signal as 200 or 300 μ for higher S/N. Since the duration of the FID signals is much shorter than both the longitudinal relaxation time of the electron spin ($T_1^e \approx 3.5$ ms [32]), and traversal relaxation time of ^{13}C (estimated longer than T_1^e [9]), we cannot observe the clear decay of the signals. In the process of Fourier transformation, we added certain window functions and zero filling to improve the spectra. Therefore we cannot observe such relaxation times from the linewidths of the resonance lines in Figs. 2 (e-f).

[1] G. Kurizki, P. Bertet, Y. Kubo, K. Mølmer, D. Petrosyan, P. Rabl, and J. Schmiedmayer, Quantum tech-

nologies with hybrid systems, Proceedings of the Na-

Operation	Spin	x	y	z
U_c	Electron	-0.0068	0.1272	0.0008
U_c	^{13}C	-0.0788	-0.3626	0.4734
U_p	Electron	0.0004	-0.0016	0.0004
U_p	^{13}C	0.0698	-0.0608	0.9920
U_{90}	Electron	0.0160	-0.0622	0.9690
U_{90}	^{13}C	0.1618	-0.9154	0.2810

TABLE IV: The x , y and z components of the final states on the Bloch sphere shown in Fig. 1.

- tional Academy of Sciences **112**, 3866 (2015).
- [2] D. Suter and F. Jelezko, Single-spin magnetic resonance in the nitrogen-vacancy center of diamond, *Progress in Nuclear Magnetic Resonance Spectroscopy* **98-99**, 50 (2017).
- [3] M. A. Nielsen and I. L. Chuang, *Quantum Computation and Quantum Information* (Cambridge University Press, Cambridge, 2000).
- [4] J. Stolze and D. Suter, *Quantum Computing: A Short Course from Theory to Experiment* (Wiley-VCH, Berlin, 2nd edition, 2008).
- [5] T. D. Ladd, F. Jelezko, R. Laflamme, Y. Nakamura, C. Monroe, and J. L. O'Brien, Quantum computers, *Nature* **464**, 45 (2010).
- [6] M. Blencowe, Quantum computing: Quantum RAM, *Nature* **468**, 44 (2010).
- [7] J. Cai, F. Jelezko, and M. B. Plenio, Hybrid sensors based on color centers in diamond and piezoactive layers, *Nature Communications*, **5**, 4065 (2014).
- [8] K. R. K. Rao and D. Suter, Characterization of hyperfine interaction between an NV electron spin and a first-shell ^{13}C nuclear spin in diamond, *Phys. Rev. B* **94**, 060101 (2016).
- [9] J. H. Shim, I. Niemeyer, J. Zhang, and D. Suter, Room-temperature high-speed nuclear-spin quantum memory in diamond, *Phys. Rev. A* **87**, 012301 (2013).
- [10] P. Cappellaro, L. Jiang, J. S. Hodges, and M. D. Lukin, Coherence and control of quantum registers based on electronic spin in a nuclear spin bath, *Phys. Rev. Lett.* **102**, 210502 (2009).
- [11] T. van der Sar, Z. H. Wang, M. S. Blok, H. Bernien, T. H. Taminiau, D. M. Toyli, D. A. Lidar, D. D. Awschalom, R. Hanson, and V. V. Dobrovitski, Decoherence-protected quantum gates for a hybrid solid-state spin register, *Nature* **484**, 82 (2012).
- [12] J. Zhang and D. Suter, Experimental protection of two-qubit quantum gates against environmental noise by dynamical decoupling, *Phys. Rev. Lett.* **115**, 110502 (2015).
- [13] M. Chen, M. Hirose, and P. Cappellaro, Measurement of transverse hyperfine interaction by forbidden transitions, *Phys. Rev. B* **92**, 020101 (2015).
- [14] N. Khaneja, Switched control of electron nuclear spin systems, *Phys. Rev. A* **76**, 032326 (2007).
- [15] C. D. Aiello and P. Cappellaro, Time-optimal control by a quantum actuator, *Phys. Rev. A* **91**, 042340 (2015).
- [16] J. S. Hodges, J. C. Yang, C. Ramanathan, and D. G. Cory, Universal control of nuclear spins via anisotropic hyperfine interactions, *Phys. Rev. A* **78**, 010303 (2008).
- [17] Y. Zhang, C. A. Ryan, R. Laflamme, and J. Baugh, Coherent control of two nuclear spins using the anisotropic hyperfine interaction, *Phys. Rev. Lett.* **107**, 170503 (2011).
- [18] T. H. Taminiau, J. J. T. Wagenaar, T. van der Sar, F. Jelezko, V. V. Dobrovitski, and R. Hanson, Detection and control of individual nuclear spins using a weakly coupled electron spin, *Phys. Rev. Lett.* **109**, 137602 (2012).
- [19] T. H. Taminiau, J. Cramer, T. van der Sar, V. V. Dobrovitski, and R. Hanson, Universal control and error correction in multi-qubit spin registers in diamond, *Nature Nanotechnology* **9**, 171 (2014).
- [20] F. Wang, Y.-Y. Huang, Z.-Y. Zhang, C. Zu, P.-Y. Hou, X.-X. Yuan, W.-B. Wang, W.-G. Zhang, L. He, X.-Y. Chang, et al., Room-temperature storage of quantum entanglement using decoherence-free subspace in a solid-state spin system, *Phys. Rev. B* **96**, 134314 (2017).
- [21] G.-Q. Liu, H. C. Po, J. Du, R.-B. Liu and X.-Y. Pan, Noise-resilient quantum evolution steered by dynamical decoupling, *Nature Communications* **4**: 2254 (2013).
- [22] J. Zhang, J. H. Shim, I. Niemeyer, T. Taniguchi, T. Teraji, H. Abe, S. Onoda, T. Yamamoto, T. Ohshima, J. Isoya, et al., Experimental implementation of assisted quantum adiabatic passage in a single spin, *Phys. Rev. Lett.* **110**, 240501 (2013).
- [23] T. Teraji, T. Taniguchi, S. Koizumi, Y. Koide, and J. Isoya, Effective use of source gas for diamond growth with isotopic enrichment, *Applied Physics Express* **6**, 055601 (2013).
- [24] M. Mitchell, *An Introduction to Genetic Algorithms* (MIT Press, Cambridge, MA, USA, 1998).
- [25] C. A. Ryan, J. S. Hodges, and D. G. Cory, Robust decoupling techniques to extend quantum coherence in diamond, *Phys. Rev. Lett.* **105**, 200402 (2010).
- [26] C. A. Ryan, C. Negrevergne, M. Laforest, E. Knill, and R. Laflamme, Liquid-state nuclear magnetic resonance as a testbed for developing quantum control methods, *Phys. Rev. A* **78**, 012328 (2008).
- [27] J. Cramer, N. Kalb, M. A. Rol, B. Hensen, M. S. Blok, M. Markham, D. J. Twitchen, R. Hanson, and T. H. Taminiau, Repeated quantum error correction on a continuously encoded qubit by real-time feedback, *Nature Communications* **7**, 11526 (2016).
- [28] A. Dreau, P. Spinicelli, J. R. Maze, J.-F. Roch, and V. Jacques, Single-shot readout of multiple nuclear spin qubits in diamond under ambient conditions, *Phys. Rev. Lett.* **110**, 060502 (2013).
- [29] D. Pagliero, A. Laraoui, J. D. Henshaw, and C. A. Meriles, Recursive polarization of nuclear spins in diamond at arbitrary magnetic fields, *Appl. Phys. Lett.* **105**, 242402 (2014).
- [30] T. Chakraborty, J. Zhang, and D. Suter, Polarizing the electronic and nuclear spin of the NV-center in diamond in arbitrary magnetic fields: analysis of the optical pumping process, *New J. Phys.* **19**, 073030 (2017).
- [31] N. Xu, Y. Tian, B. Chen, J. Geng, X. He, Y. Wang, and J. Du, Dynamically polarizing spin register of N-V centers in diamond using chopped laser pulses, *Phys. Rev. Applied* **12**, 024055 (2019).
- [32] J. Zhang, S. S. Hegde, and D. Suter, Pulse sequences for controlled two- and three-qubit gates in a hybrid quantum register, *Phys. Rev. A* **98**, 042302 (2018).
- [33] L. M. K. Vandersypen and I. L. Chuang, NMR techniques for quantum control and computation, *Rev. Mod. Phys.* **76**, 1037 (2004).

- [34] C. Zu, W.-B. Wang, L. He, W.-G. Zhang, C.-Y. Dai, F. Wang and L.-M. Duan, Experimental realization of universal geometric quantum gates with solid-state spins, *Nature*, **514**, 72 (2014).
- [35] W.-B Wang, C. Zu, L. He, W.-G. Zhang and L.-M. Duan, Memory-built-in quantum cloning in a hybrid solid-state spin register, *Sci. Rep.* **5**, 12203 (2015)
- [36] J.-P. Tetienne, L. Rondin, P. Spinicelli, M. Chipaux, T. Debuisschert, J.-F. Roch, and V. Jacques, Magnetic-field-dependent photodynamics of single NV defects in diamond: an application to qualitative all-optical magnetic imaging, *New J. Phys.* **14**, 103033 (2012).
- [37] C. S. Shin, M. C. Butler, H.-J. Wang, C. E. Avalos, S. J. Seltzer, R.-B. Liu, A. Pines, and V. S. Bajaj, Optically detected nuclear quadrupolar interaction of ^{14}N in nitrogen-vacancy centers in diamond, *Phys. Rev. B* **89**, 205202 (2014).
- [38] X.-F. He, N. B. Manson, and P. T. H. Fisk, Paramagnetic resonance of photoexcited N-V defects in diamond. II. Hyperfine interaction with the ^{14}N nucleus *Phys. Rev. B* **47**, 8816 (1993).
- [39] B. Yavkin, G. Mamin, and S. Orlinskii, High-frequency pulsed ENDOR spectroscopy of the NV^- center in the commercial HPHT diamond, *J. Magn. Reson.* **262**, 15 (2016).

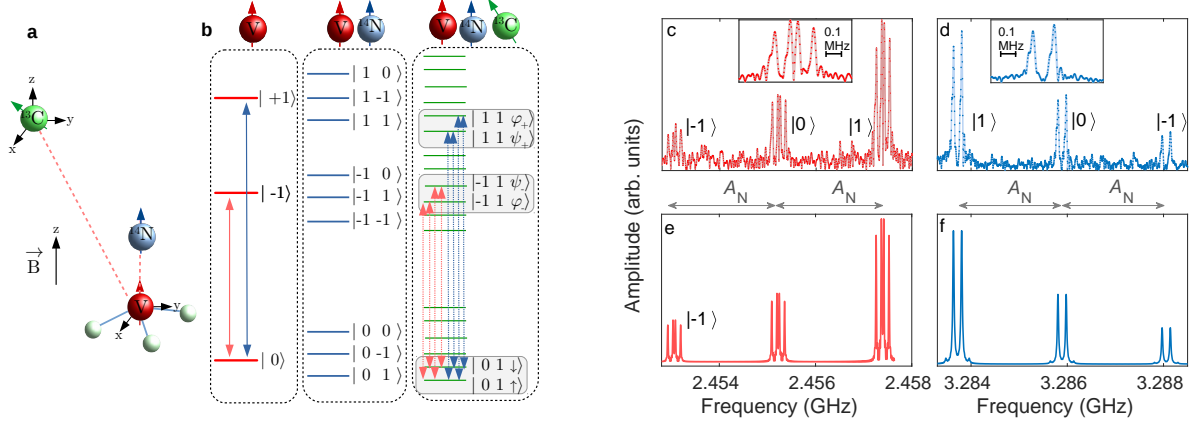


FIG. 6: Characteristics of the system. (a) Structure of the NV system with the electron spin coupled to one ^{14}N and one ^{13}C nuclear spin. (b) Energy levels of the system consisting of the electron, ^{14}N and ^{13}C nuclear spins. The vertical double arrows indicate the ESR transitions that we use in this work. (c, d) Experimental ESR spectra obtained in a field of $B = 14.8$ mT for the transitions between the $m_S = 0 \leftrightarrow -1$ and $m_S = 0 \leftrightarrow +1$ levels, respectively. The labels $|0\rangle$, $|1\rangle$, and $|-1\rangle$ mark the state of the ^{14}N spin. The insets show the peaks corresponding to the ^{14}N state $|1\rangle$ on an expanded scale. The horizontal double arrows indicate the hyperfine coupling with ^{14}N . The spectra in (e, f) show the matching numerical simulations. The small outer peaks in the simulated spectrum in figure (f) are below the noise levels in the experimental spectrum.

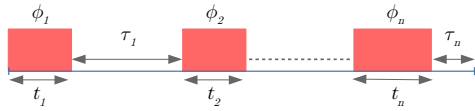


FIG. 7: Pulse sequence and variables considered for the numerical search. Here t_1, \dots, t_n are the durations and ϕ_1, \dots, ϕ_n the phases of the MW pulses and τ_1, \dots, τ_n are the delays between them. The amplitude of the pulses is fixed with a Rabi frequency $\omega_1/(2\pi) = 0.5$ MHz.

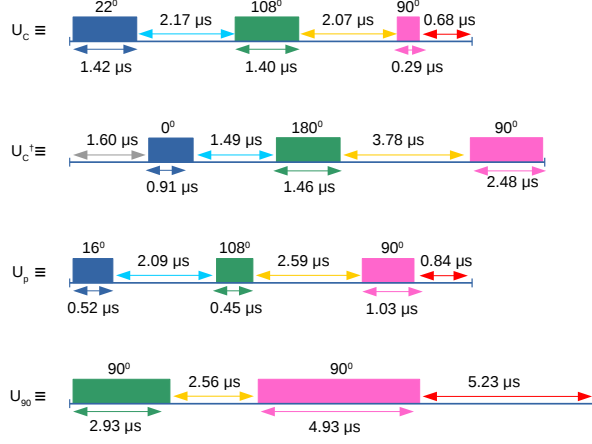


FIG. 8: Pulse sequences for U_c , U_c^\dagger , U_p and U_{90} at a fixed $\omega_1/(2\pi) = 0.5$ MHz. The MW pulses are solid rectangles and are resonant with the ESR transition $0 \leftrightarrow -1$. The phases of the pulses are indicated on the top of the rectangles.

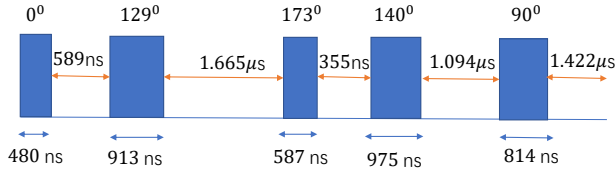


FIG. 9: Pulse sequence for U_p for $\theta_- = 36.6^\circ$, when $\nu_C = 0.3$ MHz, at a fixed $\omega_1/(2\pi) = 0.5$ MHz.

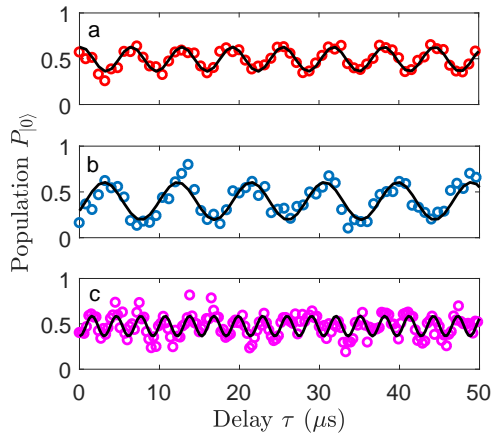


FIG. 10: The initial parts of the FIDs shown in Fig. 5, with (a-c) corresponding to Figs. 5 (a), (c) and (e), respectively.

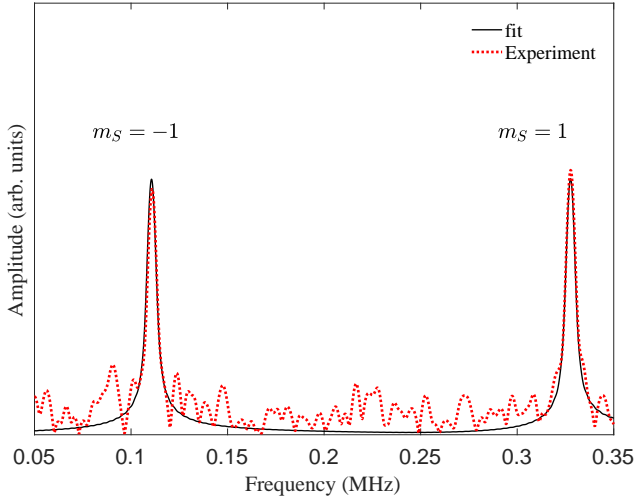


FIG. 11: Experimental and theoretical ^{13}C spin spectra corresponding to the pulse sequence in Fig. 2(f) of the main text. Here the theoretical spectrum is scaled by a factor of 0.7 to fit the experimental spectra.

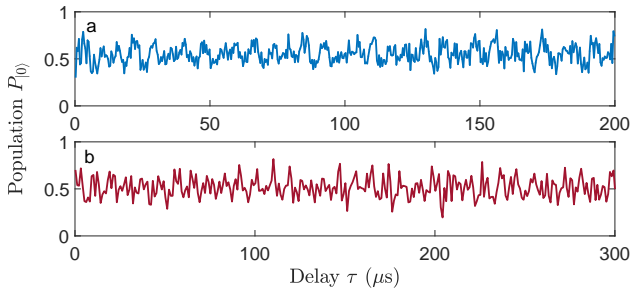


FIG. 12: (a-b) ^{13}C FID signals obtained by the pulse sequences shown in Figs. 2 (a) and (c). The spectra shown in Fig. 2 (e-f) were obtained by Fourier transformation of these signals.